Adjoint sensitivity analysis method based on lattice Boltzmann equation for flow-induced sound problems

Kusano, Kazuya
Department of Mechanical Engineering, Kyushu University

出版情報：Computers and fluids. 248, pp.105662-, 2022-11-15. Elsevier
バージョン：
権利関係：

Adjoint sensitivity analysis method based on lattice Boltzmann equation for flow-induced sound problems

Kazuya Kusano

Department of Mechanical Engineering, Kyushu University, 744 Motooka, Nishi-ku, Fukuoka, 819-0395, Japan

E-mail address: kusano@mech.kyushu-u.ac.jp

Abstract

This paper proposes an adjoint sensitivity analysis method that enables the evaluation of the sensitivities of far-field sounds with respect to object shapes. In this method, flow-induced sounds are directly simulated based on the lattice Boltzmann equation (LBE) with an athermal model under low-Mach-number conditions. In addition, wall boundaries of complex geometries are considered using the interpolated bounce-back (IBB) condition, which also allows the adoption of arbitrary parameters that define object geometries as design variables in the sensitivity analysis. The sensitivities of far-field sounds to numerous design variables can be evaluated by solving the adjoint equation, which is derived from the LBE with the IBB condition. This study demonstrates the validity of the proposed method using two test problems. In these tests, the sensitivities evaluated by the adjoint method are compared with those evaluated by the finite difference method. Furthermore, this paper presents new shapes optimized to suppress the generation of the Aeolian tone using the sensitivity analysis method.

Keywords

Computational aeroacoustics, Lattice Boltzmann method, Adjoint method, Interpolated bounce-back, Aeolian tone, Shape optimization

1. Introduction

Flow-induced sound is an important problem in the aerodynamic design of industrial products, such as vehicles and turbomachines. To address such problems, computational aeroacoustics (CAA) has advanced in the past several decades. In early studies, hybrid approaches [1,2] based on Lighthill's acoustic analogy [3] have been developed for low-Mach-number flows, which are encountered in mechanical engineering. Recently, the lattice Boltzmann method (LBM) has been gaining substantial attention as an alternative approach, which enables the direct simulation of flow and acoustic fields even under low-Mach-number conditions [4–7]. Although the advancement of CAA allows engineers to predict the aerodynamic sound and elucidate its generation mechanism in the design process, creating shapes that efficiently suppress aerodynamically sound generation remains a major challenge.

A promising approach to this challenge is shape optimization based on CAAs. Flow-induced sound problems, which include unsteady and multiscale phenomena, require expensive computational costs to evaluate design proposals. Therefore, it is unfeasible to explore the global optimum solution using evolutionary algorithms for flow-induced problems. A practical approach for such problems is gradient-based optimization aimed at obtaining a local optimum solution. In gradient-based optimization using the traditional finite differencing approach, the computational cost of evaluating the gradients of the objective function is proportional to the number of design variables. This restricts the degree of freedom of the shape.

To overcome such difficulties, the adjoint method has been proposed [8,9]. In this method, the sensitivities of an objective function with respect to all considered design variables can be efficiently evaluated by solving the adjoint equation. The computational cost is comparable to that of a single flow simulation. Numerous studies have been conducted on the adjoint method based on the Navier–Stokes equations, and several of them have attempted aeroacoustic shape optimization using hybrid approaches [10,11].

Compared to the adjoint method based on the Navier–Stokes equations, the study on the adjoint method in the LBM framework has a relatively short history. The adjoint method was initially introduced into the LBM to optimize the parameters of a collision model [12]. In addition, an adjoint sensitivity analysis based on the LBM was developed for the topology optimization of steady flow problems [13]. However, this method requires large-scale matrix operations, which deteriorate the computational efficiency of the LBM. This drawback was overcome by deriving the adjoint equation, which can be computed by a similar algorithm to the LBM [14,15]. Subsequently, the adjoint LBM has been applied to various shape and topology optimizations owing to its easy treatment for complex geometries [16–19]. However, the adjoint LBM has not yet been applied to flow-induced sound problems.

This paper presents an adjoint sensitivity analysis method based on the lattice Boltzmann equation (LBE) for flow-induced sound problems. In this method, the flow and acoustic fields are directly simulated by the LBM, where the interpolated bounce-back (IBB) condition [20–23] is used to consider complex geometries. Because the IBB condition clearly represents the object surfaces, it can be more effective for aeroacoustic optimizations than conventional optimization approaches based on a porous media model [13,16–18].The sensitivity of flow-induced sounds with respect to the design variables can be evaluated by solving the adjoint equation derived from the LBE with the IBB condition.

The remainder of this paper is organized as follows. Section 2 outlines the fluid analysis method based on the LBM. Section 3 presents the adjoint sensitivity analysis method for flow-induced sound problems. Section 4 provides two test cases, including the shape optimizations. Finally, the main findings are summarized in Section 5.

2. Fluid analysis method

2.1. Lattice Boltzmann equation

Although the LBM is a second-order scheme, it is recognized as a promising method for direct aeroacoustic simulations [7]. In fact, the LBM is less dispersive than the classical second-order Navier-Stokes scheme [4,6]. Furthermore, the number of operations per iteration and the stencil size of the LBM are smaller than those of high-order differencing schemes. These features allow the LBM to efficiently perform direct aeroacoustic simulations with parallel computing.

The LBM simulates fluid flows by computing the streaming and collision processes of particles with a finite number of velocities. In this study, the D2Q9 athermal model shown in Fig. 1 was used as a discrete velocity set. Because the temperature change is negligible in low-Mach-number flows, the athermal model can approximately simulate flow-induced sounds [6,24,25]. The discrete velocities $\mathbf{c}_i$ of the D2Q9 model are defined as follows:

$$[\mathbf{c}_i] = [\mathbf{c}_0, \mathbf{c}_1, \cdots, \mathbf{c}_8] = c\begin{bmatrix} 0 & 1 & 0 & -1 & 0 & 1 & -1 & -1 & 1 \\ 0 & 0 & 1 & 0 & -1 & 1 & 1 & -1 & -1 \end{bmatrix}. \tag{1}$$

The distribution function of a particle with velocity $\mathbf{c}_i$ at position $\mathbf{x}$ and time t is denoted by $f_i(\mathbf{x}, t)$. The evolution of the distribution functions is solved using the LBE. The LBE with the Bhatnagar–Gross–Krook model [26,27] is expressed as follows:

$$f_i(\mathbf{x} + \Delta t\mathbf{c}_i, t + \Delta t) = f_i(\mathbf{x}, t) - \frac{1}{\tau}\left[f_i(\mathbf{x}, t) - f_i^{\mathrm{eq}}(\mathbf{x}, t)\right], \tag{2}$$

where f_i^{eq} is the local equilibrium distribution function, and τ is the relaxation time. The right-hand side of Eq. (2) is the collision operator, which assumes that the particles relax to local equilibrium states at a constant rate. The time increment Δt satisfies the relation $\Delta x = \Delta tc$ where Δx is the grid spacing, implying that the CFL number is enforced to be 1 in the LBM.

In the D2Q9 model, the local equilibrium velocity distribution function f_i^{eq} is given by

$$f_i^{\mathrm{eq}} = w_i\rho\left[1 + \frac{\mathbf{c}_i \cdot \mathbf{u}}{c_s^2} + \frac{(\mathbf{c}_i \cdot \mathbf{u})^2}{4c_s^2} - \frac{\mathbf{u} \cdot \mathbf{u}}{2c_s^2}\right], \tag{3}$$

where ρ and $\mathbf{u}$ are the density and velocity of the fluid, respectively. w_i is the weighting factor, which is defined as $w_0 = 4/9$, $w_{1\sim4} = 1/9$, $w_{5\sim8} = 1/36$. $c_s = c/\sqrt{3}$ is the speed of the sound. The relaxation time τ is related to the fluid kinematic viscosity υ as follows:

$$\tau = \frac{1}{2} + \frac{\upsilon}{\Delta tc_s^2}. \tag{4}$$

Macroscopic variables, such as density ρ and velocity $\mathbf{u}$ are obtained from the particle velocity moments of the distribution functions as follows:

$$\rho = \sum_i f_i, \qquad \rho\mathbf{u} = \sum_i f_i \mathbf{c}_i. \tag{5}$$

In the athermal models, the fluid pressure is related to the density as $p = \rho c_s^2$.

2.2. Interpolated bounce-back condition

To accurately represent complex geometries using the LBM with a Cartesian grid, a special treatment is required. In this study, the IBB scheme [20–23] was used for the wall boundary condition.

The IBB approach can consider boundaries located between grid nodes by interpolating the distribution function on the boundaries based on the bounce-back rule. In this study, the linear interpolation scheme proposed by Yu et al. [22] was used. This scheme is expressed as follows:

$$f_{\bar{\imath}}(\mathbf{x}_b, t+\Delta t) = \frac{q_i}{1+q_i}\left[\hat{f}_i(\mathbf{x}_b, t) + \hat{f}_{\bar{\imath}}(\mathbf{x}_b, t)\right] + \frac{1-q_i}{1+q_i}\hat{f}_i(\mathbf{x}_b - \Delta t\mathbf{c}_i, t), \tag{6}$$

where $\bar{\imath}$ denotes the direction opposite to i, and $\hat{f}$ is the distribution function after the collision operation. Figure 2 illustrates the computational nodes near the wall boundary in the grid along direction i. In this figure, the black and white dots indicate the nodes in the fluid and solid, respectively. $\mathbf{x}_b$ is the closest node to the wall in the fluid, and q_i represents the distance between node $\mathbf{x}_b$ and the wall ($0 \le q_i < \Delta x$). Equation (6) gives the wall boundary condition by linear interpolation using the distribution functions at $\mathbf{x}_b$ and its adjacent node $\mathbf{x}_b - \mathbf{c}_i\Delta t$. This single scheme is valid for all values of q_i, unlike the well-known multiple schemes proposed by Bouzidi et al. [20]. Both schemes have been shown to be comparable in terms of accuracy and numerical stability [21,22].

The IBB condition has an important role not only for fluid analysis but also for sensitivity analysis. If the computational nodes are fixed, q_i depends only on object geometry. This implies that the geometric changes can be considered through q_i in the simulations. By using the IBB condition, arbitrary parameters defining the object geometries can be adopted as the design variables in the sensitivity analysis based on the adjoint method.

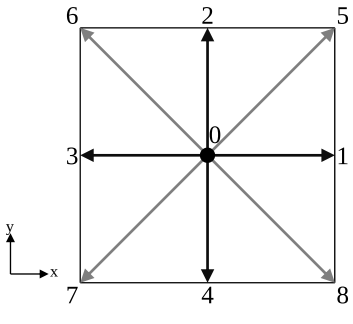

Fig. 1. D2Q9 model

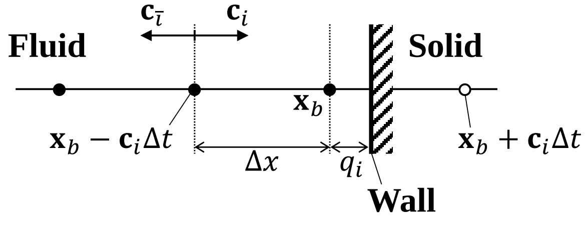

Fig. 2. Computational nodes near wall boundary

3. Sensitivity analysis method

3.1. Formulation of optimization problem

This section formulates the minimization problem for flow-induced sounds in a manner similar to that proposed by Vergnault and Sagaut [15]. In this approach constraint condition for a particle with velocity $\mathbf{c}_j$ $(j = 0,1,\cdots,8)$ at node $\mathbf{x}_k$ $(k = 1,2,\cdots,N_x)$ and time step t_n $(n = 1,2,\cdots,N_t)$ is expressed as $R_j(\mathbf{x}_k, t_n) = 0$. If X_f is defined as a subset of the computational nodes whose elements are located in the fluid, $R_j(\mathbf{x}_k, t_n)$ is expressed using the LBE (2) and the IBB condition (6), as follows:

(a) if $\mathbf{x}_k + \mathbf{c}_j \Delta t \in X_f$

$$R_j(\mathbf{x}_k, t_n) = f_j\left(\mathbf{x}_k + \Delta t \mathbf{c}_j, t_{n+1}\right) - f_j(\mathbf{x}_k, t_n) + \frac{1}{\tau}\left[f_j(\mathbf{x}_k, t_n) - f_j^{\mathrm{eq}}(\mathbf{x}_k, t_n)\right], \tag{7}$$

(b) otherwise

$$\begin{aligned} R_j(\mathbf{x}_k, t_n) = f_{\bar{j}}(\mathbf{x}_k, t_{n+1}) - \frac{q_j(\mathbf{x}_k)}{1 + q_j(\mathbf{x}_k)}\left[\hat{f}_j(\mathbf{x}_k, t_n) + \hat{f}_{\bar{j}}(\mathbf{x}_k, t_n)\right] \\ - \frac{1 - q_j(\mathbf{x}_k)}{1 + q_j(\mathbf{x}_k)}\hat{f}_j\left(\mathbf{x}_k - \Delta t \mathbf{c}_j, t_n\right). \end{aligned} \tag{8}$$

These equations indicate that the constraint condition is switched depending on whether the streaming destination of a particle is a fluid or solid region.

The objective function I is defined as the square mean of the sound pressure in an arbitrary observation region and at an arbitrary observation time:

$$I = \frac{1}{|X_{\mathrm{obs}}||T_{\mathrm{obs}}|}\sum_{\mathbf{x}_k \in X_{\mathrm{obs}}}\sum_{t_n \in T_{\mathrm{obs}}}\{p(\mathbf{x}_k, t_n) - p_0\}^2, \tag{9}$$

where X_{obs} indicates a class consisting of nodes where the observation is conducted, and T_{obs} indicates a class consisting of time steps when the observation is conducted. p_0 is the reference pressure.

The design variables, which are selected from arbitrary parameters defining object geometries, are denoted by $\alpha_m\,(m = 1,2,\cdots,N_\alpha)$. The sensitivity of the objective function I with respect to design variables α_m is written as

$$\frac{dI}{d\alpha_m} = \frac{\partial I}{\partial \alpha_m} + \frac{\partial I}{\partial f}\frac{\partial f}{\partial \alpha_m}. \tag{10}$$

$\partial f/\partial \alpha_m$ in Eq. (10) can be evaluated by conducting two flow simulations for different values of α_m and calculating the difference between these results. However, performing such an approach becomes difficult as the number of design variables N_α increases.

In this study, the optimization problem was formulated using the Lagrange multiplier method. This approach enables the evaluation of the sensitivities of the objective function to numerous design variables without repeating the flow simulations. The Lagrangian J is defined as follows:

$$J = I + \sum_j \sum_k \sum_n f_j^*(\mathbf{x}_k, t_{n+1}) R_j(\mathbf{x}_k, t_n), \tag{11}$$

where $f_j^*(\mathbf{x}_k, t_{n+1})$ are the adjoint states (Lagrange multiplier). Using the adjoint state f^*, the sensitivity of the objective function I to design variables α_m is given as follows:

$$\frac{dI}{d\alpha_m} = \frac{\partial J}{\partial \alpha_m} = \frac{\partial I}{\partial \alpha_m} + \sum_j \sum_k \sum_n f_j^*(\mathbf{x}_k, t_{n+1}) \frac{\partial R_j(\mathbf{x}_k, t_n)}{\partial \alpha_m}. \tag{12}$$

Here, the adjoint state f^* at an arbitrary node $\mathbf{x}_{k_0}$, time t_{n_0}, and discrete velocity $\mathbf{c}_i$ satisfies the following equation.

$$\frac{\partial J}{\partial f_i(\mathbf{x}_{k_0}, t_{n_0})} = \frac{\partial I}{\partial f_i(\mathbf{x}_{k_0}, t_{n_0})} + \sum_j \sum_k \sum_n f_j^*(\mathbf{x}_k, t_{n+1}) \frac{\partial R_j(\mathbf{x}_k, t_n)}{\partial f_i(\mathbf{x}_{k_0}, t_{n_0})} = 0. \tag{13}$$

Equation (13) presents the adjoint equation, as shown in the following sections. By solving the derived adjoint equation numerically, the adjoint state f^* is obtained, and the sensitivity is calculated by substituting f^* into Eq. (12).

3.2. Adjoint equation for inner nodes

In this subsection, the adjoint equation is presented for computational nodes that are free from the influence of the IBB condition. These nodes are located more than $2\Delta x$ away from the wall. By substituting Eq. (7) into Eq. (13) and executing derivative operations, the following adjoint equation is obtained (see appendix A and [15] for details) .

$$\begin{aligned} & f_i^*(\mathbf{x}_{k_0} - \Delta t \mathbf{c}_i, t_{n_0}) \\ & \quad = f_i^*(\mathbf{x}_{k_0}, t_{n_0+1}) + \frac{1}{\tau}\left[f_i^*(\mathbf{x}_{k_0}, t_{n_0+1}) - f_i^{*,\mathrm{eq}}(\mathbf{x}_{k_0}, t_{n_0+1})\right] \\ & \quad - \frac{\partial I}{\partial f_i(\mathbf{x}_{k_0}, t_{n_0})}. \end{aligned} \tag{14}$$

Here, $f_i^{*,\mathrm{eq}}$ is the local equilibrium distribution function for the adjoint equation (14) and is defined as follows:

$$f_i^{*,\mathrm{eq}} = \rho^* + \frac{(\mathbf{c}_i - \mathbf{u}) \cdot \mathbf{j}^*}{c_s^2}, \tag{15}$$

where ρ^* and $\mathbf{j}^*$ are given by

$$\rho^* = \sum_j w_j f_j^* \left[1 + \frac{\mathbf{c}_j \cdot \mathbf{u}}{c_s^2} + \frac{(\mathbf{c}_j \cdot \mathbf{u})^2}{2c_s^4} - \frac{\mathbf{u} \cdot \mathbf{u}}{2c_s^2}\right], \tag{16}$$

$$\mathbf{j}^* = \sum_j w_j f_j^* \left[\left(1 + \frac{\mathbf{c}_j \cdot \mathbf{u}}{c_s^2}\right)\mathbf{c}_j - \mathbf{u}\right]. \tag{17}$$

Furthermore, the last term in Eq. (14) can be expressed by using Eq. (9) as

$$\frac{\partial I}{\partial f_i(\mathbf{x}_{k_0}, t_{n_0})} = \begin{cases} 2c_s^4(\rho - \rho_0)/|X_{\mathrm{obs}}||T_{\mathrm{obs}}|, & \text{if } \mathbf{x}_{k_0} \in X_{\mathrm{obs}} \text{ and } t_{n_0} \in T_{\mathrm{obs}} \\ 0, & \text{otherwise} \end{cases}. \tag{18}$$

As shown in Eq. (14), the adjoint equation has a form similar to that of the LBE (2). This implies that the adjoint equation can be computed as easily as the LBM. Note that particles in the adjoint equation go backward in space and time against those in the LBE. In addition, the calculation of Eqs. (15)–(17) requires the flow velocity $\mathbf{u}$. Therefore, the instantaneous velocity data must be stored for all computational nodes for all the observation time steps in the fluid simulation.

3.3. Adjoint equation for boundary nodes

In this subsection, the adjoint equation is derived for the nodes located near the wall boundaries and affected by the IBB condition. The IBB condition (8) contains the distribution function after the collision operation at the boundary node and its neighbor node. Therefore, several terms originating from the IBB condition appear in the adjoint equation for particles that are not directly imposed by the IBB condition at these nodes.

By substituting Eqs. (7) and (8) into Eq. (13) and executing the derivative operation, the following adjoint equations are obtained: here, $\partial I/\partial f = 0$ is used because sounds are observed in regions away from the wall boundaries. The adjoint equation is as follows (see appendix A for a detailed derivation):

(a) if $\mathbf{x}_{k_0} - \Delta t\mathbf{c}_i \notin X_f$

$$\begin{aligned} f_{\bar{i}}^*(\mathbf{x}_{k_0}, t_{n_0}) &= f_i^*(\mathbf{x}_{k_0}, t_{n_0+1}) + \frac{1}{\tau}\left[f_i^*(\mathbf{x}_{k_0}, t_{n_0+1}) - f_i^{*,\mathrm{eq}}(\mathbf{x}_{k_0}, t_{n_0+1})\right] \\ &\quad + \frac{q_{\bar{i}}(\boldsymbol{x}_{k_0})}{1 + q_{\bar{i}}(\boldsymbol{x}_{k_0})}\left(1 - \frac{1}{\tau}\right) f_{\bar{i}}^*(\boldsymbol{x}_{k_0}, t_{n_0+1}) + \chi_i(\boldsymbol{x}_{k_0}, t_{n_0+1}) \\ &\quad + \psi_i(\boldsymbol{x}_{k_0}, t_{n_0+1}), \end{aligned} \tag{19}$$

(b) otherwise

$$\begin{aligned} f_i^*(\mathbf{x}_{k_0} - \Delta t\mathbf{c}_i, t_{n_0}) \\ &= f_i^*(\mathbf{x}_{k_0}, t_{n_0+1}) + \frac{1}{\tau}\left[f_i^*(\mathbf{x}_{k_0}, t_{n_0+1}) - f_i^{*,\mathrm{eq}}(\mathbf{x}_{k_0}, t_{n_0+1})\right] \\ &\quad + \chi_i(\mathbf{x}_{k_0}, t_{n_0+1}) + \psi_i(\mathbf{x}_{k_0}, t_{n_0+1}), \end{aligned} \tag{20}$$

where χ and ψ are given as follows:

$$\begin{aligned} \chi_i(\mathbf{x}_{k_0}, t_{n_0+1}) = \sum_{\tilde{\mathbf{x}}_{kj} \in X_{b1}} \frac{1}{1 + q_j(\mathbf{x}_k)} f_j^*(\mathbf{x}_k, t_{n_0+1}) \Bigg[-\left(1 - \frac{1}{\tau}\right) \delta_{\mathbf{x}_k, \mathbf{x}_{k_0}} \delta_{j,i} \\ - \frac{1}{\tau}\frac{\partial f_j^{\mathrm{eq}}}{\partial f_i} \delta_{\mathbf{x}_k, \mathbf{x}_{k_0}} + q_j(\mathbf{x}_k) \frac{1}{\tau}\frac{\partial f_{\bar{j}}^{\mathrm{eq}}}{\partial f_i} \delta_{\mathbf{x}_k, \mathbf{x}_{k_0}} \Bigg], \end{aligned} \tag{21}$$

$$\psi_i(\mathbf{x}_{k_0}, t_{n_0+1}) = \sum_{\tilde{\tilde{\mathbf{x}}}_{kj} \in X_{b2}} \frac{1 - q_j(\mathbf{x}_k + \Delta t\mathbf{c}_j)}{1 + q_j(\mathbf{x}_k + \Delta t\mathbf{c}_j)} f_j^*(\mathbf{x}_k + \Delta t\mathbf{c}_j, t_{n_0+1}) \left[\left(1 - \frac{1}{\tau}\right) \delta_{\mathbf{x}_k, \mathbf{x}_{k_0}} \delta_{i,j} + \frac{1}{\tau} \frac{\partial f_j^{\mathrm{eq}}}{\partial f_i} \delta_{\mathbf{x}_k, \mathbf{x}_{k_0}} \right]. \tag{22}$$

Here, X_{b1} and X_{b2} are the computational elements defined as

$$X_{b1} = \{\tilde{\mathbf{x}}_{kj} \mid \tilde{\mathbf{x}}_{kj} \notin X_f, \mathbf{x}_k \in X_f\}, \tag{23}$$

$$X_{b2} = \{\tilde{\tilde{\mathbf{x}}}_{kj} \mid \tilde{\tilde{\mathbf{x}}}_{kj} \notin X_f, \tilde{\mathbf{x}}_{kj} \in X_f\}, \tag{24}$$

where $\tilde{\mathbf{x}}_{kj} = \mathbf{x}_k + \Delta t\mathbf{c}_j$ and $\tilde{\tilde{\mathbf{x}}}_{kj} = \mathbf{x}_k + 2\Delta t\mathbf{c}_j$. In addition, $\partial f_j^{\mathrm{eq}}/\partial f_i$ in Eqs. (21) and (22) are calculated as follows [15]:

$$\frac{\partial f_j^{\mathrm{eq}}}{\partial f_i} = w_j \left\{ 1 + \frac{\mathbf{c}_j \cdot \mathbf{u}}{c_s^2} + \frac{(\mathbf{c}_j \cdot \mathbf{u})^2}{2c_s^4} - \frac{\mathbf{u} \cdot \mathbf{u}}{2c_s^2} + \frac{(\mathbf{c}_i - \mathbf{u})}{c_s^2} \cdot \left[\left(1 + \frac{\mathbf{c}_j \cdot \mathbf{u}}{c_s^2}\right) \mathbf{c}_j - \mathbf{u} \right] \right\}. \tag{25}$$

Eq. (19) corresponds to the wall boundary condition for the adjoint equation (14). For other particles located within $2\Delta x$ from the wall, Eq. (20) is constituted by adding the terms χ and ψ originated from the IBB condition to the adjoint equation (14). For inner nodes located more than $2\Delta x$ away from the wall, Eq. (20) is reduced to Eq. (14).

In a previous study, Cheylan et al. formulated the adjoint equation for the IBB condition [19]. In their formula, these additional terms are not considered because the adjoint equations for the inner and boundary nodes are derived independently. In the present study, the adjoint equations were formulated to exactly satisfy Eq. (13), even near the wall boundary, which may evaluate the sensitivity more accurately.

3.4. **Evaluation of sensitivity**

After computing the adjoint equation, the sensitivities can be calculated by substituting the adjoint state f^* into Eq. (12), which is transformed using q_j as follows:

$$\frac{dI}{d\alpha_m} = \sum_j \sum_k \sum_n f_j^*(\mathbf{x}_k, t_{n+1}) \frac{\partial R_j(\mathbf{x}_k, t_n)}{\partial q_j} \frac{\partial q_j}{\partial \alpha_m}, \tag{26}$$

where $\partial I/\partial \alpha_m = 0$ is used because the observation region is not set near the object. By substituting Eqs. (7) and (8) into Eq. (23) and executing the derivative operation, $\partial R_j(\mathbf{x}_k, t_n)/\partial q_j$ is expressed as follows:

$$\frac{\partial R_j(\mathbf{x}_k, t_n)}{\partial q_j} = \begin{cases} \dfrac{-1}{(1+q_j)^2} \left[\hat{f}_j(\mathbf{x}_k, t_n) + \hat{f}_{\bar{j}}(\mathbf{x}_k, t_n)\right] + \dfrac{2}{(1+q_j)^2} \hat{f}_j(\mathbf{x}_k - \Delta t\mathbf{c}_j, t_n), & \text{if } \mathbf{x}_k + \Delta t\mathbf{c}_j \notin X_f \\ 0, & \text{otherwise} \end{cases}. \tag{27}$$

$\partial q_j/\partial \alpha_m$ in Eq. (26) can be numerically calculated at a low computational cost.

4. **Numerical examples**

This section presents two numerical examples to demonstrate the validity of the proposed method. One is the sound propagation around a flat plate (acoustic barrier) in a fluid at rest, and the other is the Aeolian tone generated from a bluff body in uniform flow. In these validations, the sensitivities evaluated by the adjoint method were compared with those evaluated by the finite difference method.

4.1. **Acoustic barrier**

The first test was conducted for a simple acoustic problem concerning an acoustic barrier in a fluid at rest. As shown in Fig.3, a synthetic sound source was placed in a domain surrounded by a wall. The domain size was $8\ \mathrm{m} \times 8\ \mathrm{m}$. The observation point, where the objective function I was evaluated, was placed 2 m away from the sound source. In addition, a flat plate was installed in the center between the sound source and the observation point as an acoustic barrier, which interrupted the sound propagation from the sound source to the observation point. The width of the flat plate was 0.20 m, and the flat plate length L was varied in the range of $0.16\ \mathrm{m} \leq L \leq 1.4$ m. The flat plate length L was considered as the design variable in this test problem, and the sensitivity of the objective function I with respect to the flat plate length L was evaluated.

In the fluid simulation, the sound was generated by adding a source term to Eq. (2) at the location of the sound source as follows:

$$f_i(\mathbf{x} + \Delta t\mathbf{c}_i, t + \Delta t) = f_i(\mathbf{x}, t) - \frac{1}{\tau}\left[f_i(\mathbf{x}, t) - f_i^{\mathrm{eq}}(\mathbf{x}, t)\right] + w_i\rho_s \sin(2\pi f_s t). \tag{28}$$

The amplitude ρ_s was set as $\rho_s = 1.0 \times 10^{-2}\rho_0$, where ρ_0 is the reference density. For the sound source frequency f_s, three conditions of 2, 4, and 8 kHz were considered.

The domain was discretized into 1025^2 grid points. The time increment Δt was 1.3×10^{-5} s. The fluid kinematic viscosity υ was set to $0.005\ \mathrm{m}^2/\mathrm{s}$. The initial condition was uniformly given by the local equilibrium distribution function calculated from the conditions of $\rho = \rho_0$ and $\mathbf{u} = \mathbf{0}$. The fluid simulations were completed before the sounds that reflected off the outer walls reached the observation point. The total number of time steps was 800 for the fluid and adjoint simulations.

Figure 4 plots the relationship between the flat plate length L and the objective function I. In this figure, the objective function I was normalized using the maximum value I_{max}. The figure shows that as the flat plate length L increases, the sound propagation toward the observation point is interrupted more effectively, and the objective function I decreases exponentially. Moreover, the curve naturally depends on the sound frequency f_s, owing to the difference in the diffraction effect.

Figure 5 compares the evaluated sensitivities of the objective function I with respect to the flat plate length L between the adjoint method and the finite difference method. Note that in the finite difference method, the sensitivities were evaluated by avoiding the conditions where the edges of the flat plate exactly coincide with the grid lines, because the IBB condition is not continuous around $q_i = 0$. In addition to the exact adjoint equation, the present study tested for the approximated equation, where the terms χ_i and ψ_i were neglected in equation (20). Such an approximation was involved in the formulation proposed by the previous study [19].

As shown in Fig. 5, the sensitivity also depends on the flat plate length L and sound frequency f_s. In terms of these points, the sensitivities evaluated by the proposed method agreed well with those evaluated by the finite difference method. The maximum value of the relative error for the exact equation was 0.038%. These results suggest that the formulation of the proposed adjoint method using the IBB condition is correct. Furthermore, the exact equation provides better results than the approximated equation, implying that the proposed formulation is more accurate than the existing one.

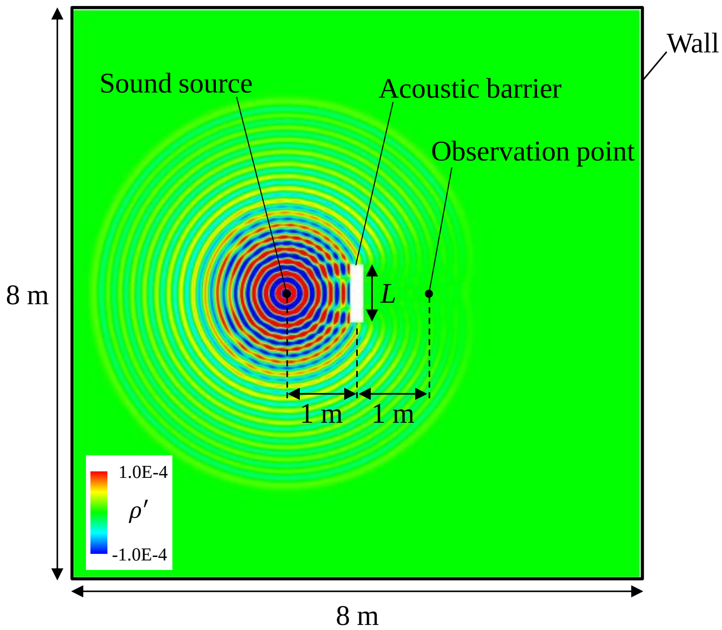

Fig. 3. Computational domain for the acoustic barrier and an instantaneous contour of density fluctuation.

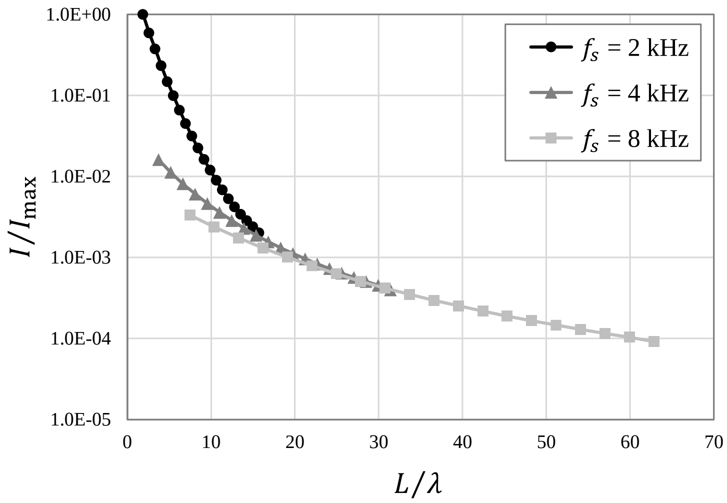

Fig. 4. Objective function calculated for various lengths of the acoustic barrier

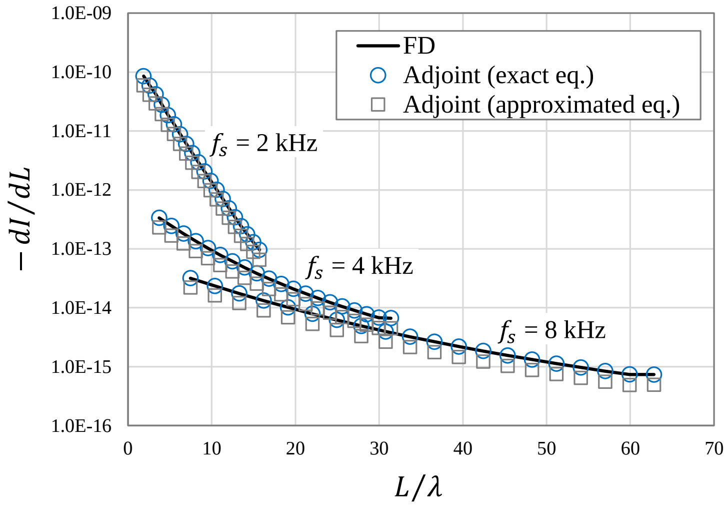

Fig. 5. Sensitivity of the objective function to the length of the acoustic barrier

4.2. Aeolian tone of a bluff body

4.2.1. Computational setup

Second, the proposed method was applied to the Aeolian tone of a cylinder in uniform flow, and the sensitivity evaluated using the adjoint method was validated. Furthermore, the shape of the cylinder was optimized using sensitivity analysis.

The object shape was defined by an Akima spline [28] using 21 control points. In the initial shape, the control points were evenly spaced on a circle of diameter D, as shown in Fig. 6. The shape was symmetrical with respect to the x-axis, which was parallel to the free stream. The circumferential position θ_m of each point was fixed, and the radial position r_m of each point was considered as the design variable. In the shape optimization, the design variables α_m were modified using the gradient descent method according to the sensitivity analysis results, as follows:

$$
{\alpha_m}^{h+1} = {\alpha_m}^{h} - \eta \frac{dI}{d\alpha_m}, \tag{29}
$$

where superscript h indicates the number of updates. The step size η was fixed at $\eta/(D^2/I_0) = 0.03$, where I_0 is the objective function calculated for the initial shape. The value was determined after some trials to obtain converged shapes. By using the adjoint method, this study can explore more complex geometries compare with past optimizations for the Aeolian tone of a bluff body [29,30].

In this problem, the Mach number of the uniform flow was 0.2, and the Reynolds number based on the circular cylinder diameter *D* was 150. The computational domain was a square with a side of 2048*D*, as shown in Fig. 7. This domain was sufficiently large to capture the waves of the Aeolian tone, the wavelength of which was estimated as 27*D* under this flow condition. As shown in Fig. 7, the domain was divided into 400 sub-domains, each of which contains 131×131 grid points. The fine grids were arranged near the cylinder, and the smallest grid spacing was 0.0154*D*. To enable the LBM simulation using locally refined grids, the distribution function was interpolated and rescaled at the interface between two differently sized grids using a multi-scale approach [31,32]. This method was validated for the Aeolian tone of a circular cylinder in a previous report [6].

To prevent sound reflection from the outer boundaries, sound waves were absorbed in the region defined as $r > 768D$, where r is the radial coordinate. In this region, the damping term [33] is added to Eq. (1) as follows:

$$
\begin{aligned}
&f_i(\mathbf{x} + \Delta t \mathbf{c}_i, t + \Delta t) \\
&\quad = f_i(\mathbf{x}, t) - \frac{1}{\tau}\left[f_i(\mathbf{x}, t) - f_i^{\mathrm{eq}}(\mathbf{x}, t)\right] - \alpha \left(\frac{x_d}{L_d}\right)^2 \left[f_i^{\mathrm{eq}}(\mathbf{x}, t) - f_i^{\infty}(\mathbf{x}, t)\right],
\end{aligned} \tag{30}
$$

where L_d indicates the width of the absorbing region in the radial direction, and x_d indicates the distance from the inner boundary of the absorbing region. In this study, L_d was 256*D*, which is sufficiently large to include nine wavelengths or more in the radial direction. f_i^{∞} is the local equilibrium function calculated from the free-stream density and velocity. Parameter α was set to 0.05. In addition, the adjoint equation (14) was modified for the absorbing region as follows:

$$
\begin{aligned}
&f_i^*\left(\mathbf{x}_{k_0} - \Delta t \mathbf{c}_i, t_{n_0}\right) \\
&\quad = f_i^*\left(\mathbf{x}_{k_0}, t_{n_0+1}\right) + \frac{1}{\tau}\left[f_i^*\left(\mathbf{x}_{k_0}, t_{n_0+1}\right) - f_i^{*,\mathrm{eq}}\left(\mathbf{x}_{k_0}, t_{n_0+1}\right)\right] \\
&\quad - \alpha \left(\frac{x_d}{L_d}\right)^2 f_i^{*,\mathrm{eq}}\left(\mathbf{x}_{k_0}, t_{n_0+1}\right).
\end{aligned} \tag{31}
$$

The observation lines, where the objective function was evaluated, were defined as shown in Fig. 8. The lines were installed along the computational grid to surround the cylinder, except for downstream of the cylinder. Downstream of the cylinder, pressure fluctuations are generated not only by sound waves, but also by the wake flow. The distance between the cylinder and observation lines was defined as L_{obs}. The observation was initiated at the 250,000th time step from the start of the calculation, after periodic fluctuations were observed in the flow and acoustic fields. In this test, the effects of the position and duration of the observation on the sensitivity evaluation were investigated.

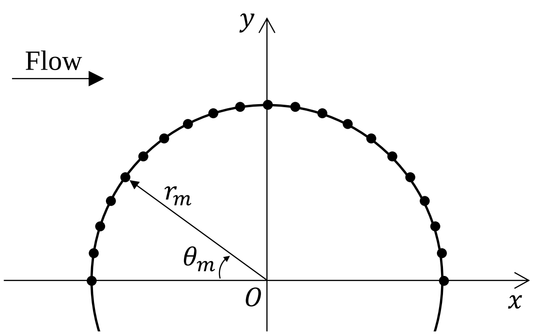

Fig. 6. Geometry definition

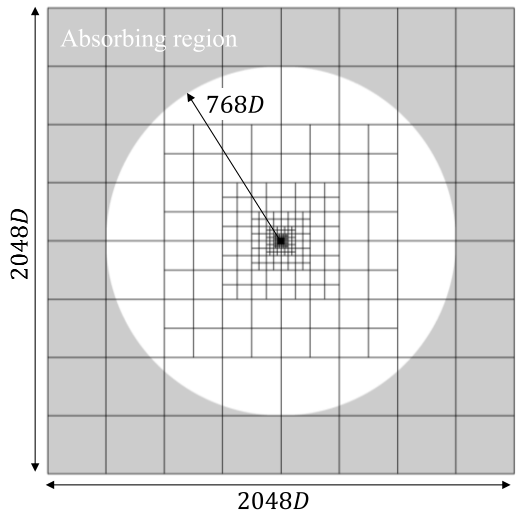

Fig. 7. Computational domain for bluff body's Aeolian tone

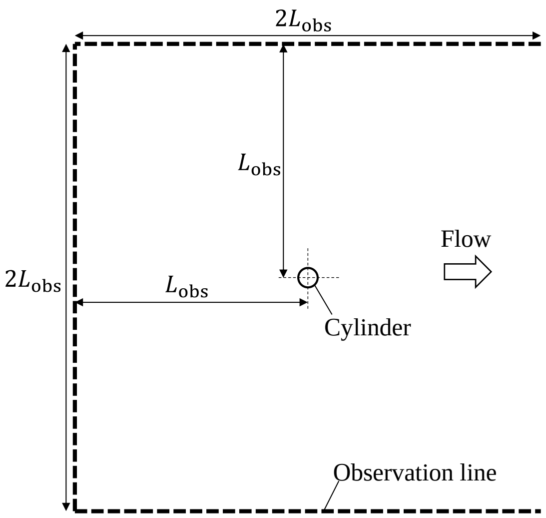

Fig. 8. Observation position for the Aeolian tone of a cylinder

4.2.2. **Sensitivity analysis results**

In this subsection, the sensitivity analysis results are discussed. Figures 9–11 show the sensitivity distributions of objective function I with respect to r_m along the circumferential direction for the initial circular shape.

First, the effect of the observation position, which is specified by L_{obs} as shown in Fig. 8, on the sensitivity evaluation was investigated. For this purpose, the observation time was fixed to 16 times longer than the vortex shedding period. As shown in Fig. 8, in the case of $L_{\text{obs}}/D < 20$, the peak of the sensitivity appears near $\theta = 80°$, which corresponds to the separation point. For $L_{\text{obs}}/D \geq 20$, the peak of sensitivity appears near $\theta = 100°$. These sensitivity distributions tend to converge as the observation position is away from the object. These results indicate that the sensitive part of the object for the far-field sound is different from that for the near-field sound. Therefore, optimization using the near-field sound as the objective function may result in a shape different from the optimization using the far-field sound. In the following results, the observation position was set to $L_{\text{obs}}/D = 20$.

Second, the effect of the observation time on the sensitivity evaluation is shown in Fig. 10. In the figure, the observation time T^*_{obs} is defined as $T^*_{\text{obs}} = |T_{\text{obs}}|\Delta t$, and the vortex shedding period T_v is given by $T_v = D/(S_t U_\infty)$, where U_∞ is the free-stream velocity and S_t is the Strouhal number calculated from the time variations of the lift. Figure 10 shows that the absolute values of the sensitivity were underestimated when the observation time was short. As the observation time increased, the sensitivity distributions tended to converge. Longer observations require not only a longer computational time, but also a larger storage capacity. In the following results, including the shape optimizations, the observation time was set as $T^*_{\text{obs}}/T_v = 16$ considering both accuracy and computational cost.

Next, sensitivities evaluated using the adjoint method and finite difference method were compared for the conditions of $L_{\text{obs}}/D = 20$ and $T^*_{\text{obs}}/T_v = 16$ (Fig.11). Although the absolute value of the sensitivity was slightly underestimated by the adjoint method because of the short observation time, the distributions agreed well in both results. The relative error of the gradient vector $\nabla I = [dI/d\alpha_1, dI/d\alpha_2, \cdots, dI/d\alpha_m]^T$ was 19.2%, which was calculated as $\|\nabla I_{\text{Adjoint}} - \nabla I_{\text{FD}}\|/\|\nabla I_{\text{FD}}\|$. The accuracy of the sensitivity analysis should be sufficient to perform shape optimization using the gradient descent method, in which the direction of the gradient vector is more important than the individual values. These results demonstrate that the proposed method can directly evaluate the sensitivity of the far-field sound with respect to the object shapes. To the best of author's knowledge, this is the first case in which such sensitivity was successfully evaluated by the adjoint LBM.

Finally, information about computational cost is presented. Table 1 summarizes the execution time of the fluid and the sensitivity analysis for $T^*_{\text{obs}}/T_v = 16$, which corresponds to 50,000 time steps. The calculations were performed in parallel using 400 cores. These data indicate that the computational times per time step of the LBM and adjoint calculations were comparable. Furthermore, the proposed method required 74% of the total execution time to save and reload the velocity data. Consequently, the total execution time increased by approximately five times compared with the LBM calculation alone. These facts suggest that the proposed adjoint method can evaluate sensitivities faster than the conventional finite difference method for five or more design variables. However, to temporarily store the velocity data for all 6.9 million grid points over 50,000 time steps, SSDs with a capacity of 5.5TB or more were required, which is a problem that needs to be addressed for practical applications.

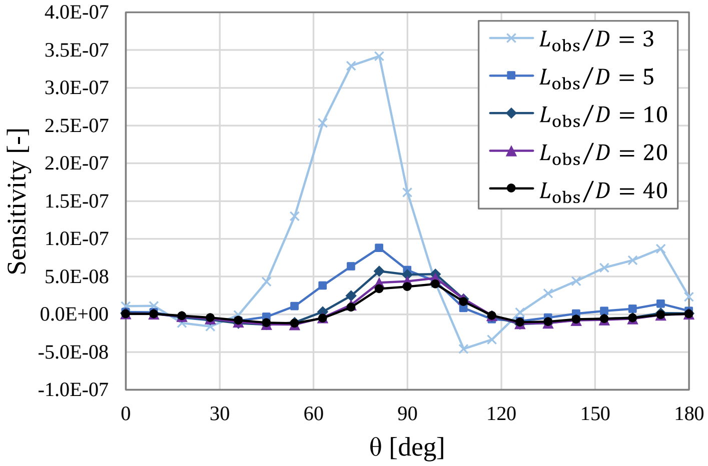

Fig. 9. Effect of the observation position on the sensitivity evaluation for the Aeolian tone.

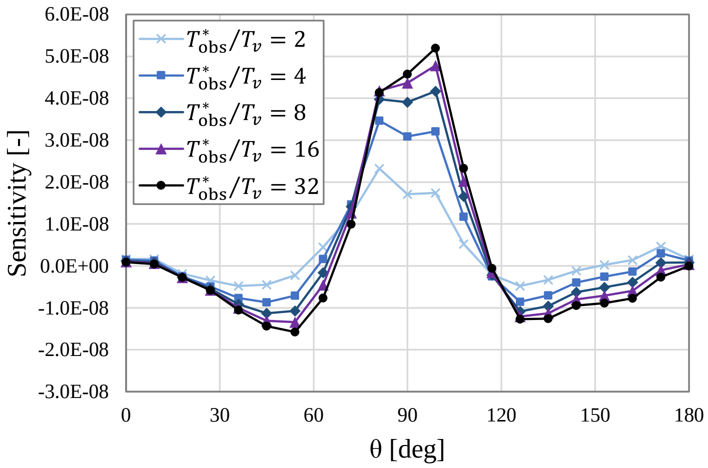

Fig. 10. Effect of the observation time on the sensitivity evaluation for the Aeolian tone.

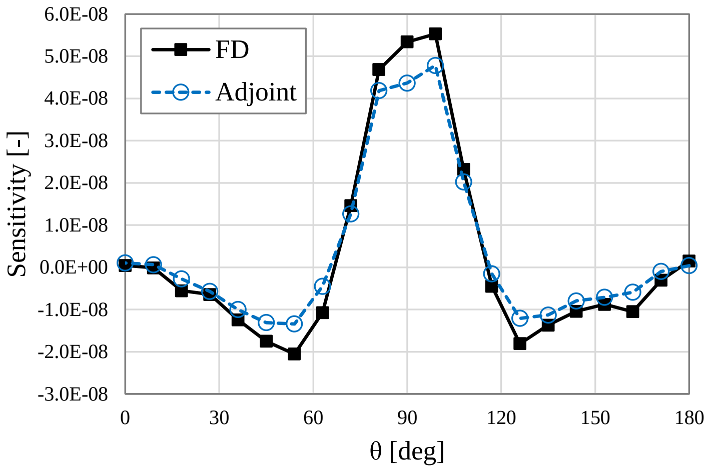

Fig. 11. Comparison of the sensitivity distributions evaluated by the adjoint method and finite difference method.

Table 1. Run-time of the fluid and sensitivity analysis for the aeolian tone using 400 cores.

Processing	Time steps	Run-time [min]
LBM calculation	300,000	9.4
Adjoint calculation	50,000	2.1
Saving and reloading velocity data	50,000	33.0
Total	-	44.5

4.2.3. Shape optimization results

Shape optimizations were performed for two cases with different numbers of design variable, N_α. One considered only 5 control points near the trailing edge as design variables, and the other points were fixed. The other case considered all 21 control points as the design variables.

Figure 12 shows the convergence processes of the objective function in the optimizations. In this figure, the change in the sound pressure level $\Delta\mathrm{SPL}$ is defined as follows:

$$\Delta\mathrm{SPL} = 10\log_{10}\frac{I}{I_0}, \tag{32}$$

where I_0 is the objective function evaluated for the initial shape. As the number of optimization iterations increased, the sound pressure level decreased monotonically in both cases. Both cases converged within 30 iterations. After 30 iterations, the sound pressure level was totally reduced by 2.7 and 6.3 dB in the case of $N_\alpha = 5$ and 21, respectively.

The optimized shapes were compared with the initial shape in Fig. 13. In the case of $N_\alpha = 5$, a horn-like projection was generated from the surface near $\theta = 150°$. This case achieved sound reduction by locally changing the shape on the downstream side. This new shape is different from any known shapes, such as splitter plates [34–36]. In the case of $N_\alpha = 21$, the shape changed significantly from the bluff body to a streamlined one. This result is consistent with that of a previous study [37]. Although there were no constraints, the positions of the leading and trailing edges were almost unchanged from the initial positions in this case.

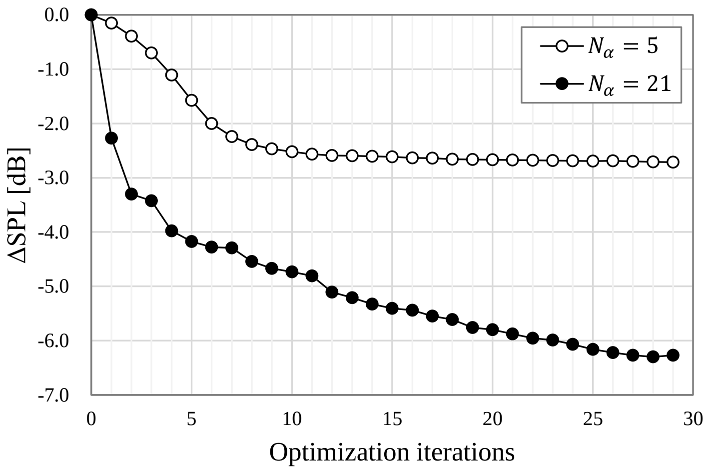

Fig. 12. Optimization convergence histories.

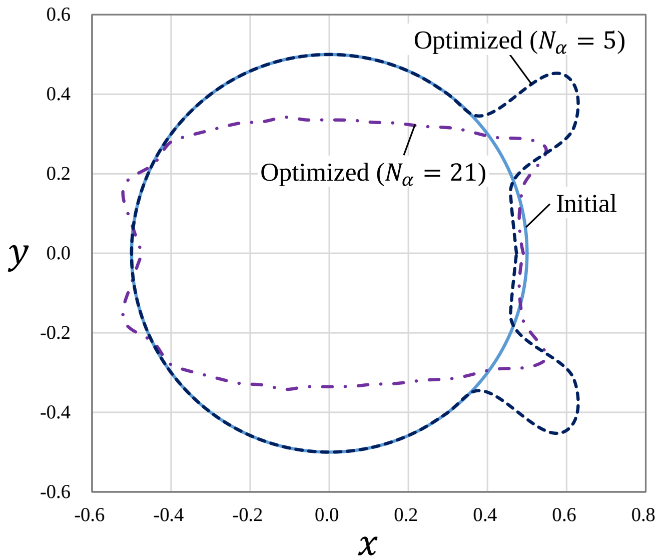

Fig. 13. Initial and Optimized shapes

In the following, the flow and acoustic fields are compared between the initial and optimized shapes. The aeolian tone is mainly contributed by lift fluctuations [38]. Figure 14 shows the time variations of the lift coefficient for the initial and optimized shapes, where time t is normalized with the cylinder diameter and the free-stream velocity, and $t = 0$ corresponds to a positive peak of the lift in each result. In the initial shape, the amplitude and Strouhal number for the lift fluctuation were 0.527 and 0.182, respectively. These values are close to the numerical results reported by Inoue and Hatakeyama, where the amplitude was 0.52, and the Strouhal number was 0.183 for the same flow condition [38]. In the optimization cases of $N_\alpha = 5$ and 21, the amplitude was significantly reduced to 0.255 and 0.066, respectively. In addition, for $N_\alpha = 5$, the Strouhal number was slightly decreased to 0.179 by generating the projections. Conversely, for $N_\alpha = 21$, the Strouhal number was increased to 0.220 according to the reduction in the wake width. The above values of the amplitude and Strouhal number for the lift fluctuation are summarized in Table 2, where the mean values of the drag coefficient are also shown. Even an optimized shape with projections can reduce mean drag.

Figure 15 shows instantaneous contours of the pressure fluctuation around the initial and optimized shapes at $t = 0$. As shown in Fig. 15 (a), negative and positive pressure fluctuations are generated alternately over the upper and lower side of the circular cylinder. These dipole sounds propagate in a direction that is inclined slightly upstream from the y direction due to the Doppler effect [38]. Although these sound generation and propagation processes are also observed around the optimized shapes in Fig. 15 (b) and (c), the sound radiation from these optimized shapes is smaller for all directions than that from the initial shape. These results suggest that the sound generation is suppressed by the optimized shapes.

Figure 16 shows instantaneous vorticity distribution around the initial and optimized shapes at $t = 0$. The Karman vortex street is observed in the wake behind each body. As shown in Fig. 16 (a), the vortex rolled up near the rear surface of the circular cylinder, inducing the significant lift fluctuation. A comparison between Fig. 16 (a) and (b) reveals that the vortex formation is delayed by the projections of the optimized shape. This shape may restrict unsteady behaviors of the separated shear layers near the body, suppressing the lift fluctuation and the sound generation. Furthermore, Fig. 16 (a) and (c) indicate that the vortices shed from the optimized shape ($N_\alpha = 21$) is weaker than those from the initial shape. In addition, the vortex-shedding direction of the optimized shape ($N_\alpha = 21$) is more inclined to the streamwise direction compared with the initial shape. These flow changes are mainly attributed to the decrease in the curvature of the upper and lower surfaces, and the flow acceleration over the surfaces is relaxed in the optimized shape compared with the initial shape. Consequently, the lift fluctuation and the Aeolian tone are significantly suppressed.

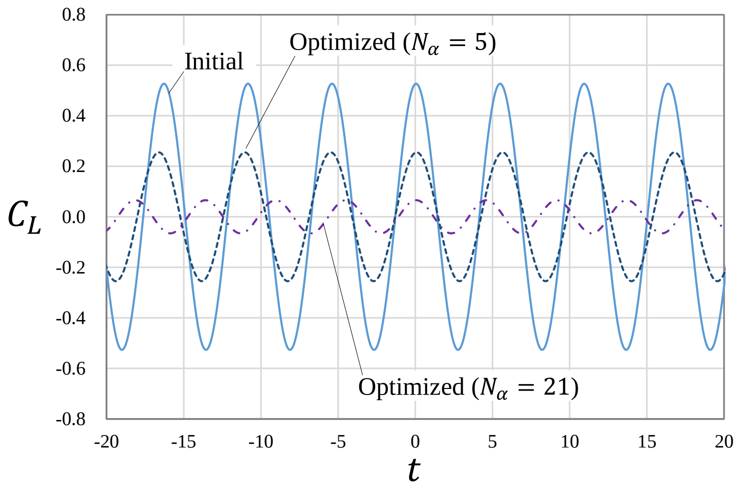

Fig. 14. Time variations of lift coefficient.

Table 2. Comparison of the mean drag coefficient, the amplitude of lift the coefficient, and the Strouhal number among initial and optimized shapes.

Autor	**Shape**	C_D	C'_L	S_t
Inoue and Hatakeyama [38]	Circular cylinder	1.34	0.52	0.183
Present	Circular cylinder	1.32	0.527	0.182
Present	Optimized (N_α = 5)	1.16	0.255	0.179
Present	Optimized (N_α = 21)	0.77	0.066	0.220

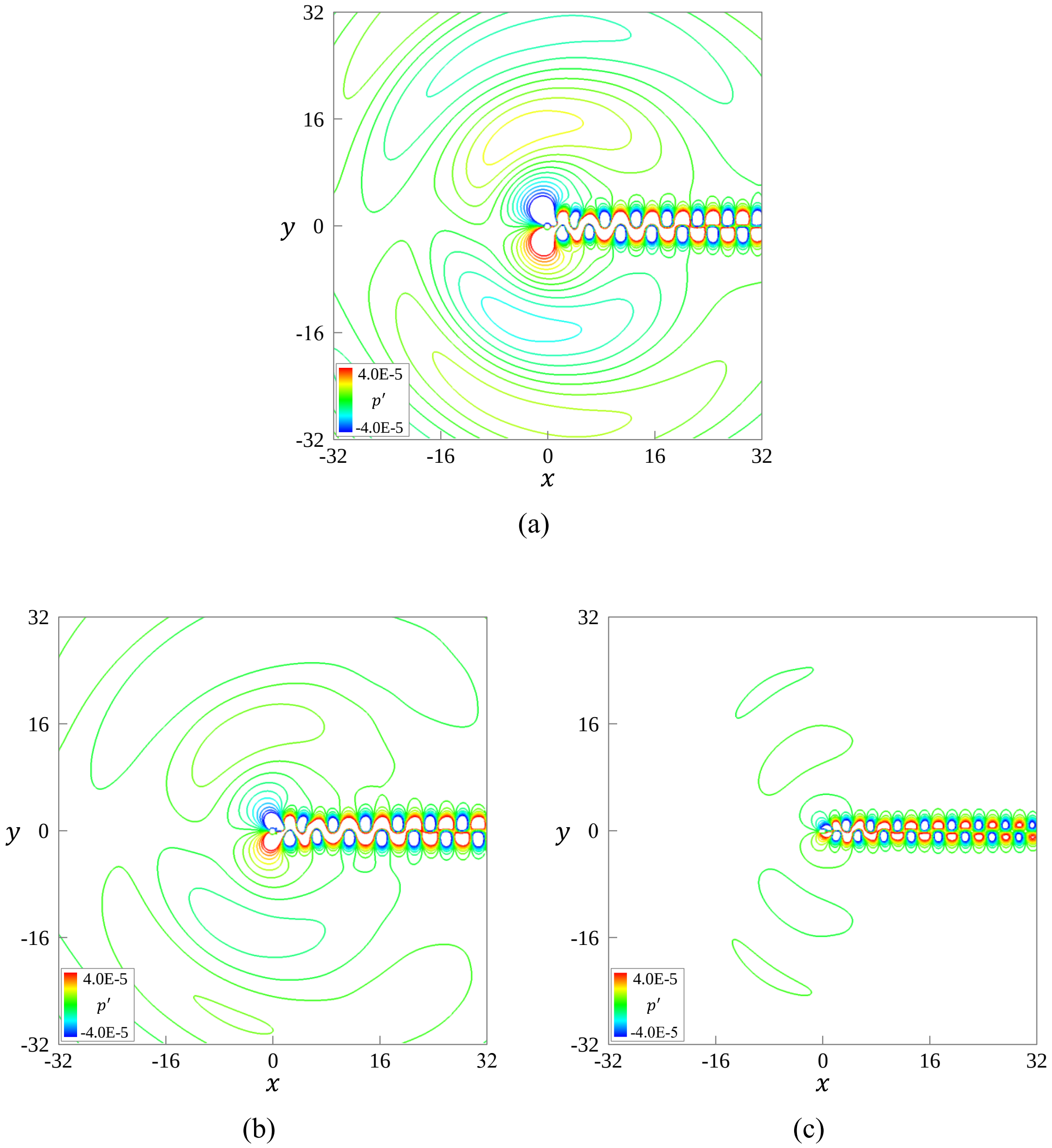

Fig. 15. Instantaneous distributions of pressure fluctuation when the lift coefficient is maximum. (a) Initial shape; (b) optimized shape ($N_\alpha = 5$); (c) optimized shape ($N_\alpha = 21$).

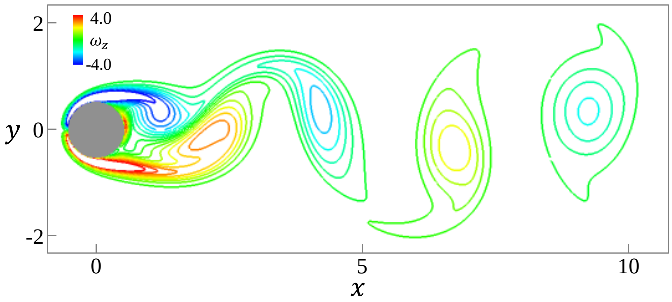

(a)

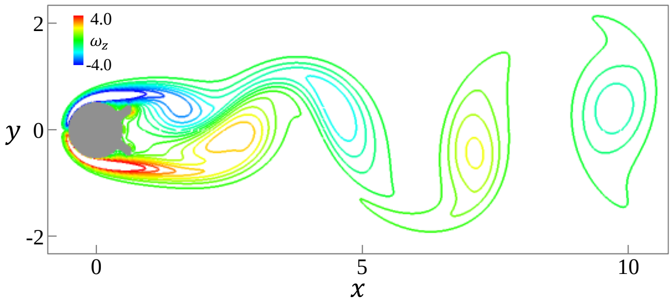

(b)

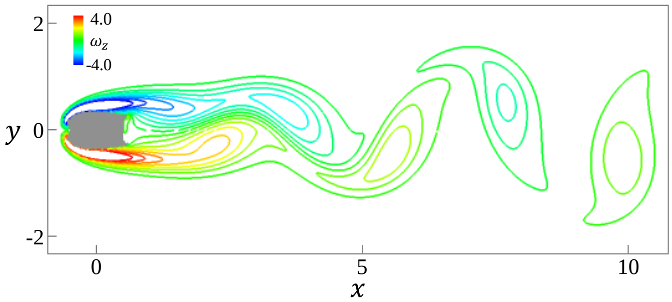

(c)

Fig. 16. Instantaneous vorticity contours when the lift coefficient is maximum. (a) Initial shape; (b) optimized shape ($N_\alpha = 5$); (c) optimized shape ($N_\alpha = 21$).

5. Conclusions

The adjoint sensitivity analysis method based on the LBE has been proposed to effectively suppress the generation of flow-induced sounds by shape optimization. In this method, the flow and acoustic fields around complex geometries are directly simulated using the LBM with the IBB condition. To efficiently evaluate the sensitivities of numerous design variables for flow-induced sounds, adjoint equations for the LBM with the IBB condition were formulated. These adjoint equations can be computed easily, similar to the LBM.

The proposed method was validated through two test problems concerning an acoustic barrier in a fluid at rest and the Aeolian tone generated from a cylinder in uniform flow. Consequently, the sensitivities evaluated by the adjoint method agreed well with those evaluated by the finite difference method. Furthermore, shape optimizations were performed to minimize the Aeolian tone, and new shapes suppressing sound generation were obtained.

6. Acknowledgment

This study was supported by JSPS KAKENHI (Grant Number JP20K22397 and JP22K03929). The author gratefully acknowledges the research fund from the Harada Memorial Foundation. Computational resources were provided by the Research Institute for Information Technology, Kyushu University.

Appendix A: Derivation of the adjoint equations

This appendix shows the detailed derivation of the adjoint equations for the LBE with Yu's IBB condition. First, Eq. (13) is rewritten by renaming the constraint condition $R_j(\mathbf{x}_k, t_n)$ in Eqs. (7) and (8) into $R_j^{\mathrm{LBE}}(\mathbf{x}_k, t_n)$ and $R_j^{\mathrm{IBB}}(\mathbf{x}_k, t_n)$, respectively, as follows:

$$\begin{aligned}&\frac{\partial I}{\partial f_i\left(\mathbf{x}_{k_0}, t_{n_0}\right)} + \sum_{\tilde{\mathbf{x}}_{kj} \notin X_{b1}} \sum_n f_j^*(\mathbf{x}_k, t_{n+1}) \frac{\partial R_j^{\mathrm{LBE}}(\mathbf{x}_k, t_n)}{\partial f_i\left(\mathbf{x}_{k_0}, t_{n_0}\right)} \\ &\quad + \sum_{\tilde{\mathbf{x}}_{kj} \in X_{b1}} \sum_n f_j^*(\mathbf{x}_k, t_{n+1}) \frac{\partial R_j^{\mathrm{IBB}}(\mathbf{x}_k, t_n)}{\partial f_i\left(\mathbf{x}_{k_0}, t_{n_0}\right)} = 0,\end{aligned} \tag{A.1}$$

where the sums of nodes and particles are combined into one using a variable defined as $\tilde{\mathbf{x}}_{kj} = \mathbf{x}_k + \Delta t \mathbf{c}_j$. X_{b1} is a subset of the computational elements, where the IBB condition is imposed, as defined by Eq. (23). The partial derivatives of $R_j^{\mathrm{LBE}}(\mathbf{x}_k, t_n)$ and $R_j^{\mathrm{IBB}}(\mathbf{x}_k, t_n)$ with $f_i\left(\mathbf{x}_{k_0}, t_{n_0}\right)$ in Eq. (A.1) can be expressed using the delta function δ as follows:

$$\frac{\partial R_j^{\mathrm{LBE}}(\mathbf{x}_k, t_n)}{\partial f_i(\mathbf{x}_{k_0}, t_{n_0})} = \delta_{\mathbf{x}_k+\Delta t\mathbf{c}_j,\mathbf{x}_{k_0}} \delta_{t_{n+1},t_{n_0}} \delta_{j,i} - \left(1 - \frac{1}{\tau}\right) \delta_{\mathbf{x}_k,\mathbf{x}_{k_0}} \delta_{t_n,t_{n_0}} \delta_{j,i} \\ - \frac{1}{\tau}\frac{\partial f_j^{\mathrm{eq}}}{\partial f_i} \delta_{\mathbf{x}_k,\mathbf{x}_{k_0}} \delta_{t_n,t_{n_0}}, \tag{A.2}$$

$$\frac{\partial R_j^{\mathrm{IBB}}(\mathbf{x}_k, t_n)}{\partial f_i(\mathbf{x}_{k_0}, t_{n_0})} = \delta_{\mathbf{x}_k,\mathbf{x}_{k_0}} \delta_{t_{n+1},t_{n_0}} \delta_{\bar{j},i} \\ - \frac{q_j(\mathbf{x}_k)}{1+q_j(\mathbf{x}_k)} \left[\left(1 - \frac{1}{\tau}\right) \delta_{\mathbf{x}_k,\mathbf{x}_{k_0}} \delta_{t_n,t_{n_0}} \delta_{j,i} + \frac{1}{\tau}\frac{\partial f_j^{\mathrm{eq}}}{\partial f_i} \delta_{\mathbf{x}_k,\mathbf{x}_{k_0}} \delta_{t_n,t_{n_0}} \right. \\ \left. + \left(1 - \frac{1}{\tau}\right) \delta_{\mathbf{x}_k,\mathbf{x}_{k_0}} \delta_{t_n,t_{n_0}} \delta_{\bar{j},i} + \frac{1}{\tau}\frac{\partial f_{\bar{j}}^{\mathrm{eq}}}{\partial f_i} \delta_{\mathbf{x}_k,\mathbf{x}_{k_0}} \delta_{t_n,t_{n_0}} \right] \\ - \frac{1-q_j(\mathbf{x}_k)}{1+q_j(\mathbf{x}_k)} \left[\left(1 - \frac{1}{\tau}\right) \delta_{\mathbf{x}_k-\mathbf{c}_j\Delta t,\mathbf{x}_{k_0}} \delta_{t_n,t_{n_0}} \delta_{j,i} \right. \\ \left. + \frac{1}{\tau}\frac{\partial f_j^{\mathrm{eq}}}{\partial f_i} \delta_{\mathbf{x}_k-\mathbf{c}_j\Delta t,\mathbf{x}_{k_0}} \delta_{t_n,t_{n_0}} \right]. \tag{A.3}$$

It was carefully considered whether or not each term in these equations remains after substituting into Eq. (A.1), as shown in the following subsections.

A.1. Derivation for inner nodes

If $\mathbf{x}_{k_0}$ is an inner node located more than $2\Delta x$ away from the wall, the second term in Eq. (A.1) is expressed as follows:

$$\sum_{\tilde{\mathbf{x}}_{kj}\notin X_{b1}} \sum_n f_j^*(\mathbf{x}_k, t_{n+1}) \frac{\partial R_j^{\mathrm{LBE}}(\mathbf{x}_k, t_n)}{\partial f_i(\mathbf{x}_{k_0}, t_{n_0})} \\ = f_i^*(\mathbf{x}_{k0} - \Delta t\mathbf{c}_i, t_{n_0}) - \left(1 - \frac{1}{\tau}\right) f_i^*(\mathbf{x}_{k_0}, t_{n_0+1}) \\ - \frac{1}{\tau}\sum_j f_j^*(\mathbf{x}_{k_0}, t_{n_0+1}) \frac{\partial f_j^{\mathrm{eq}}}{\partial f_i}(\mathbf{x}_{k_0}, t_{n_0}). \tag{A.4}$$

The third term in Eq. (A.1) is obviously zero for inner nodes. The adjoint equation (14) was obtained by expressing the last term in the Eq. (A.4) as $f_i^{*,\mathrm{eq}}(\mathbf{x}_{k_0}, t_{n_0+1})$ and substituting Eq. (A.4) into Eq. (A.1). A detailed derivation of $f_i^{*,\mathrm{eq}}$ is available in the literature [15].

A.2. Derivation for boundary nodes

Next, the cases that $\mathbf{x}_{k_0}$ is located within $2\Delta x$ from the wall are considered. For these nodes, the first term in Eq. (A.1) is zero because sounds are observed in regions distant from the wall boundaries. The particles in these nodes are divided into the following two cases.

(a) If $\mathbf{x}_{k_0} - \Delta t \mathbf{c}_i \notin X_f$

These particles require the boundary condition for the adjoint equation. For such particles, the second and third terms in Eq. (A.1) are expressed as follows:

$$\sum_{\tilde{\mathbf{x}}_{kj} \notin X_{b1}} \sum_{n} f_j^*(\mathbf{x}_k, t_{n+1}) \frac{\partial R_j^{\mathrm{LBE}}(\mathbf{x}_k, t_n)}{\partial f_i(\mathbf{x}_{k_0}, t_{n_0})}$$

$$= -\left(1 - \frac{1}{\tau}\right) f_i^*(\mathbf{x}_{k_0}, t_{n_0+1}) - \frac{1}{\tau} f_i^{*,\mathrm{eq}}(\mathbf{x}_{k_0}, t_{n_0+1}) \tag{A.5}$$

$$+ \sum_{\tilde{\mathbf{x}}_{kj} \in X_{b1}} \frac{1}{\tau} f_j^*(\mathbf{x}_k, t_{n_0+1}) \frac{\partial f_j^{\mathrm{eq}}}{\partial f_i} \delta_{\mathbf{x}_k, \mathbf{x}_{k_0}},$$

$$\sum_{\tilde{\mathbf{x}}_{kj} \in X_{b1}} \sum_{n} f_j^*(\mathbf{x}_k, t_{n+1}) \frac{\partial R_j^{\mathrm{IBB}}(\mathbf{x}_k, t_n)}{\partial f_i(\mathbf{x}_{k_0}, t_{n_0})}$$

$$= f_{\bar{\iota}}^*(\mathbf{x}_{k_0}, t_{n_0}) - \frac{q_{\bar{\iota}}(\mathbf{x}_{k_0})}{1 + q_{\bar{\iota}}(\mathbf{x}_{k_0})} \left(1 - \frac{1}{\tau}\right) f_{\bar{\iota}}^*(\mathbf{x}_{k_0}, t_{n_0+1})$$

$$+ \sum_{\tilde{\mathbf{x}}_{kj} \in X_{b1}} f_j^*(\mathbf{x}_k, t_{n_0+1}) \frac{-q_j(\mathbf{x}_k)}{1 + q_j(\mathbf{x}_k)} \left[\frac{1}{\tau} \frac{\partial f_j^{\mathrm{eq}}}{\partial f_i} \delta_{\mathbf{x}_k, \mathbf{x}_{k_0}} + \frac{1}{\tau} \frac{\partial f_{\bar{j}}^{\mathrm{eq}}}{\partial f_i} \delta_{\mathbf{x}_k, \mathbf{x}_{k_0}} \right] \tag{A.6}$$

$$- \sum_{\tilde{\mathbf{x}}_{kj} \in X_{b1}} f_j^*(\mathbf{x}_k, t_{n_0+1}) \frac{1 - q_j(\mathbf{x}_k)}{1 + q_j(\mathbf{x}_k)} \left[\left(1 - \frac{1}{\tau}\right) \delta_{\mathbf{x}_k - \mathbf{c}_j \Delta t, \mathbf{x}_{k_0}} \delta_{j,i} \right.$$

$$\left. + \frac{1}{\tau} \frac{\partial f_j^{\mathrm{eq}}}{\partial f_i} \delta_{\mathbf{x}_k - \mathbf{c}_j \Delta t, \mathbf{x}_{k_0}} \right].$$

Unlike in Eq. (A.4) for inner nodes, the last term in Eq. (A.5) appears owing to the absence of the LBE for the computational element $\tilde{\mathbf{x}}_{k_0 i}$. By using a variable defined as $\tilde{\tilde{\mathbf{x}}}_{kj} = \mathbf{x}_k + 2\Delta t \mathbf{c}_j$, the last term in Eq. (A.6) is transformed to $\psi_i(\mathbf{x}_{k_0}, t_{n_0+1})$, as shown in Eq. (22). The substitution of Eqs. (A.5) and (A.6) into Eq. (A.1) results in the following equation.

$$
\begin{aligned}
f_{\bar{i}}^{*}\left(\mathbf{x}_{k_0}, t_{n_0}\right) &- \left(1-\frac{1}{\tau}\right) f_{i}^{*}\left(\mathbf{x}_{k_0}, t_{n_0+1}\right) - \frac{1}{\tau} f_{i}^{*,\mathrm{eq}}\left(\mathbf{x}_{k_0}, t_{n_0+1}\right) \\
&- \frac{q_{\bar{i}}\left(\mathbf{x}_{k_0}\right)}{1+q_{\bar{i}}\left(\mathbf{x}_{k_0}\right)} \left(1-\frac{1}{\tau}\right) f_{\bar{i}}^{*}\left(\mathbf{x}_{k_0}, t_{n_0+1}\right) \\
&+ \sum_{\tilde{\mathbf{x}}_{kj} \in X_{b1}} f_{j}^{*}\left(\mathbf{x}_{k}, t_{n_0+1}\right) \frac{1}{1+q_{j}(\mathbf{x}_{k})} \left[\frac{1}{\tau} \frac{\partial f_{j}^{\mathrm{eq}}}{\partial f_{i}} \delta_{\mathbf{x}_k, \mathbf{x}_{k_0}} \right. \\
&\left. - q_{j}(\mathbf{x}_{k}) \frac{1}{\tau} \frac{\partial f_{\bar{j}}^{\mathrm{eq}}}{\partial f_{i}} \delta_{\mathbf{x}_k, \mathbf{x}_{k_0}} \right] - \psi_{i}\left(\mathbf{x}_{k_0}, t_{n_0+1}\right) = 0.
\end{aligned} \tag{A.7}
$$

(b) Otherwise

These particles do not require the boundary condition, but additional terms originated from the IBB conditions appear, unlike in the inner nodes. The second and third terms in Eq. (A.1) are expressed as follows:

$$
\begin{aligned}
&\sum_{\tilde{\mathbf{x}}_{kj} \notin X_{b1}} \sum_{n} f_{j}^{*}(\mathbf{x}_{k}, t_{n+1}) \frac{\partial R_{j}^{\mathrm{LBE}}(\mathbf{x}_{k}, t_{n})}{\partial f_{i}\left(\mathbf{x}_{k_0}, t_{n_0}\right)} \\
&\qquad = f_{i}^{*}\left(\mathbf{x}_{k_0} - \Delta t \mathbf{c}_{i}, t_{n_0}\right) - \left(1-\frac{1}{\tau}\right) f_{i}^{*}\left(\mathbf{x}_{k_0}, t_{n_0+1}\right) \\
&\qquad + \sum_{\tilde{\mathbf{x}}_{kj} \in X_{b1}} \left(1-\frac{1}{\tau}\right) f_{j}^{*}\left(\mathbf{x}_{k}, t_{n_0+1}\right) \delta_{\mathbf{x}_k, \mathbf{x}_{k_0}} \delta_{j,i} - \frac{1}{\tau} f_{i}^{*,\mathrm{eq}}\left(\mathbf{x}_{k_0}, t_{n_0+1}\right) \\
&\qquad + \sum_{\tilde{\mathbf{x}}_{kj} \in X_{b1}} \frac{1}{\tau} f_{j}^{*}\left(\mathbf{x}_{k}, t_{n_0+1}\right) \frac{\partial f_{j}^{\mathrm{eq}}}{\partial f_{i}} \delta_{\mathbf{x}_k, \mathbf{x}_{k_0}},
\end{aligned} \tag{A.8}
$$

$$
\begin{aligned}
&\sum_{\tilde{\mathbf{x}}_{kj} \in X_{b1}} \sum_{n} f_{j}^{*}(\mathbf{x}_{k}, t_{n+1}) \frac{\partial R_{j}^{\mathrm{IBB}}(\mathbf{x}_{k}, t_{n})}{\partial f_{i}\left(\mathbf{x}_{k_0}, t_{n_0}\right)} \\
&\qquad = \sum_{\tilde{\mathbf{x}}_{kj} \in X_{b1}} f_{j}^{*}\left(\mathbf{x}_{k}, t_{n_0+1}\right) \frac{-q_{j}(\mathbf{x}_{k})}{1+q_{j}(\mathbf{x}_{k})} \left[\left(1-\frac{1}{\tau}\right) \delta_{\mathbf{x}_k, \mathbf{x}_{k_0}} \delta_{j,i} \right. \\
&\qquad \left. + \frac{1}{\tau} \frac{\partial f_{j}^{\mathrm{eq}}}{\partial f_{i}} \delta_{\mathbf{x}_k, \mathbf{x}_{k_0}} + \frac{1}{\tau} \frac{\partial f_{\bar{j}}^{\mathrm{eq}}}{\partial f_{i}} \delta_{\mathbf{x}_k, \mathbf{x}_{k_0}} \right] - \psi_{i}\left(\mathbf{x}_{k_0}, t_{n_0+1}\right).
\end{aligned} \tag{A.9}
$$

The substitution of Eqs. (A.8) and (A.9) into Eq. (A.1) yields the following equation.

$$f_i^*(\mathbf{x}_{k_0} - \Delta t \mathbf{c}_i, t_{n_0}) - \left(1 - \frac{1}{\tau}\right) f_i^*(\mathbf{x}_{k_0}, t_{n_0+1}) - \frac{1}{\tau} f_i^{*,\mathrm{eq}}(\mathbf{x}_{k_0}, t_{n_0+1})$$

$$+ \sum_{\tilde{\mathbf{x}}_{kj} \in X_{b1}} f_j^*(\mathbf{x}_k, t_{n_0+1}) \frac{1}{1 + q_j(\mathbf{x}_k)} \left[\left(1 - \frac{1}{\tau}\right) \delta_{\mathbf{x}_k, \mathbf{x}_{k_0}} \delta_{j,i} \right. \tag{A.10}$$

$$\left. + \frac{1}{\tau} \frac{\partial f_j^{\mathrm{eq}}}{\partial f_i} \delta_{\mathbf{x}_k, \mathbf{x}_{k_0}} - q_j(\mathbf{x}_k) \frac{1}{\tau} \frac{\partial f_{\bar{j}}^{\mathrm{eq}}}{\partial f_i} \delta_{\mathbf{x}_k, \mathbf{x}_{k_0}} \right] - \psi_i(\mathbf{x}_{k_0}, t_{n_0+1}) = 0.$$

The second term to the last in Eq. (A.10) is named as $\chi_i(\mathbf{x}_{k_0}, t_{n_0+1})$. If $\mathbf{x}_{k_0} - \Delta t \mathbf{c}_i \notin X_f$, the first term of χ_i disappears, then χ_i equals to the second term to the last in Eq. (A.7). Therefore, the adjoint equations for boundary nodes can be expressed using χ_i, as shown in Eqs. (19) and (20).

References

[1] Wang M, Moin P. Computation of trailing-edge flow and noise using large-eddy simulation. AIAA J 2000;38:2201–9. https://doi.org/10.2514/2.895.

[2] Kato C, Yamade Y, Wang H, Guo Y, Miyazawa M, Takaishi T, et al. Numerical prediction of sound generated from flows with a low Mach number. Comput Fluids 2007;36:53–68. https://doi.org/10.1016/j.compfluid.2005.07.006.

[3] Lighthill MJ. On Sound Generated Aerodynamically . I . General Theory M . J . Lighthill On Sound Generated Aerodynamically . I . General Theory M . J . Lighthill Proceedings of the Royal Society of London . Series A , Mathematical and Physical Sciences , Vol . Proc R Soc London A 1952;211:564–87.

[4] Marié S, Ricot D, Sagaut P. Comparison between lattice Boltzmann method and Navier-Stokes high order schemes for computational aeroacoustics. J Comput Phys 2009;228:1056–70. https://doi.org/10.1016/j.jcp.2008.10.021.

[5] Tsutahara M. The finite-difference lattice Boltzmann method and its application in computational aero-acoustics. Fluid Dyn Res 2012;44. https://doi.org/10.1088/0169-5983/44/4/045507.

[6] Kusano K, Yamada K, Furukawa M. Aeroacoustic simulation of broadband sound generated from low-Mach-number flows using a lattice Boltzmann method. J Sound Vib 2020;467:115044. https://doi.org/10.1016/j.jsv.2019.115044.

[7] Moreau S. The third golden age of aeroacoustics The third golden age of aeroacoustics 2022;031301. https://doi.org/10.1063/5.0084060.

[8] Pironneua O. On optimum design in fluid mechanics. J Fluid Mech 1974;64:97–110.

[9] Jameson A. Aerodynamic design via control theory. J Sci Comput 1988;3:233–60. https://doi.org/10.1007/BF01061285.

[10] Kapellos CS, Papoutsis-Kiachagias EM, Giannakoglou KC, Hartmann M. The unsteady continuous adjoint method for minimizing flow-induced sound radiation. J Comput Phys 2019;392:368–84. https://doi.org/10.1016/j.jcp.2019.04.056.

[11] Zhou BY, Albring T, Gauger NR, da Silva CR, Economon TD, Alonso JJ. Efficient airframe noise reduction framework via adjoint-based shape optimization. AIAA J 2021;59:580–95. https://doi.org/10.2514/1.J058917.

[12] Tekitek MM, Bouzidi M, Dubois F, Lallemand P. Adjoint lattice Boltzmann equation for parameter identification. Comput Fluids 2006;35:805–13. https://doi.org/10.1016/j.compfluid.2005.07.015.

[13] Pingen G, Evgrafov A, Maute K. Adjoint parameter sensitivity analysis for the hydrodynamic lattice Boltzmann method with applications to design optimization. Comput Fluids 2009;38:910–23. https://doi.org/10.1016/j.compfluid.2008.10.002.

[14] Krause MJ, Thäter G, Heuveline V. Adjoint-based fluid flow control and optimisation with lattice Boltzmann methods. Comput Math with Appl 2013;65:945–60. https://doi.org/10.1016/j.camwa.2012.08.007.

[15] Vergnault E, Sagaut P. An adjoint-based lattice Boltzmann method for noise control problems. J Comput Phys 2014;276:39–61. https://doi.org/10.1016/j.jcp.2014.07.027.

[16] Yaji K, Yamada T, Yoshino M, Matsumoto T, Izui K, Nishiwaki S. Topology optimization in thermal-fluid flow using the lattice Boltzmann method. J Comput Phys 2016;307:355–77. https://doi.org/10.1016/j.jcp.2015.12.008.

[17] Nørgaard S, Sigmund O, Lazarov B. Topology optimization of unsteady flow problems using the lattice Boltzmann method. J Comput Phys 2016;307:291–307. https://doi.org/10.1016/j.jcp.2015.12.023.

[18] Dugast F, Favennec Y, Josset C, Fan Y, Luo L. Topology optimization of thermal fluid flows with an adjoint Lattice Boltzmann Method. J Comput Phys 2018;365:376–404. https://doi.org/10.1016/j.jcp.2018.03.040.

[19] Cheylan I, Fritz G, Ricot D, Sagaut P. Shape optimization using the adjoint lattice Boltzmann method for aerodynamic applications. AIAA J 2019;57:2758–73. https://doi.org/10.2514/1.J057955.

[20] Bouzidi M, Firdaouss M, Lallemand P. Momentum transfer of a Boltzmann-lattice fluid with boundaries. Phys Fluids 2001;13:3452–9. https://doi.org/10.1063/1.1399290.

[21] Yu D, Mei R, Luo LS, Shyy W. Viscous flow computations with the method of lattice Boltzmann equation. Prog Aerosp Sci 2003;39:329–67. https://doi.org/10.1016/S0376-0421(03)00003-4.

[22] Yu D, Mei R, Shyy W. A unified boundary treatment in lattice Boltzmann method. 41st Aerosp Sci Meet Exhib 2003;8. https://doi.org/10.2514/6.2003-953.

[23] Sanjeevi SKP, Zarghami A, Padding JT. Choice of no-slip curved boundary condition for lattice Boltzmann simulations of high-Reynolds-number flows. Phys Rev E 2018;97:1–10. https://doi.org/10.1103/PhysRevE.97.043305.

[24] Buick JM, Greated CA, Campbell DM. Lattice BGK simulation of sound waves. Europhys Lett 1998;43:235–40. https://doi.org/10.1209/epl/i1998-00346-7.

[25] De Jong AT, Bijl H, Hazir A, Wiedemann J. Aeroacoustic simulation of slender partially covered cavities using a Lattice Boltzmann method. J Sound Vib 2013;332:1687–703. https://doi.org/10.1016/j.jsv.2012.09.040.

[26] Chen H, Chen S, Matthaeus WH. Recovery of the Navier-Stokes equations using a lattice-gas Boltzmann method. Phys Rev A 1992;45:5339–42. https://doi.org/10.1103/PhysRevA.45.R5339.

[27] Qian YH, D'Humières D, Lallemand P. Lattice bgk models for navier-stokes equation. Epl 1992;17:479–84. https://doi.org/10.1209/0295-5075/17/6/001.

[28] Akima H. A New Method of Interpolation and Smooth Curve Fitting Based on Local Procedures. J ACM 1970;17:589–602. https://doi.org/10.1145/321607.321609.

[29] Gonçalves da Silva Pinto WJ, Margnat F. Shape optimization for the noise induced by the flow over compact bluff bodies. Comput Fluids 2020;198. https://doi.org/10.1016/j.compfluid.2019.104400.

[30] Gonçalves da Silva Pinto WJ, Margnat F. A shape optimization procedure for cylinders aeolian tone. Comput Fluids 2019;182:37–51. https://doi.org/10.1016/j.compfluid.2019.02.002.

[31] Flippova O, Hanel D. Grid Refinement for Lattice-BGK Models. J Comput Phys 1998;147:219–28.

[32] Succi S, Filippova O, Chen H, Orszag S. Towards a renormalized Lattice Boltzmann equation for fluid turbulence. J Stat Phys 2002;107:261–78. https://doi.org/10.1023/A:1014570923357.

[33] Kam EWS, So RMC, Leung RCK. Lattice boltzmann method simulation of aeroacoustics and nonreflecting boundary conditions. AIAA J 2007;45:1703–12. https://doi.org/10.2514/1.27632.

[34] Mahato B, Ganta N, Bhumkar YG. Effective control of aeolian tone using a pair of splitter plates. J Sound Vib 2021;494:115906. https://doi.org/10.1016/j.jsv.2020.115906.

[35] Ali MSM, Doolan CJ, Wheatley V. Aeolian tones generated by a square cylinder with a detached flat plate. AIAA J 2013;51:291–301. https://doi.org/10.2514/1.J051378.

[36] You D, Choi H, Choi MR, Kang SH. Control of flow-induced noise behind a circular cylinder using splitter plates. AIAA J 1998;36:1961–7. https://doi.org/10.2514/2.322.

[37] Chen W, Li X, Zhang W. Shape optimization to suppress the lift oscillation of flow past

a stationary circular cylinder. Phys Fluids 2019;31. https://doi.org/10.1063/1.5095841.

[38] Inoue O, Hatakeyama N. Sound generation by a two-dimensional circular cylinder in a uniform flow. J Fluid Mech 2002;471:285–314. https://doi.org/10.1017/S0022112002002124.